

## THE INTERMEDIATE NEUTRON-CAPTURE PROCESS AND CARBON-ENHANCED METAL-POOR STARS

MELANIE HAMPEL<sup>1,2</sup>, RICHARD J. STANCLIFFE<sup>2</sup>, MARIA LUGARO<sup>3,4</sup>, BRADLEY S. MEYER<sup>5</sup>

## ABSTRACT

Carbon-enhanced metal-poor (CEMP) stars in the Galactic Halo display enrichments in heavy elements associated with either the *s* (slow) or the *r* (rapid) neutron-capture process (e.g., barium and europium respectively), and in some cases they display evidence of both. The abundance patterns of these CEMP-*s/r* stars, which show both Ba and Eu enrichment, are particularly puzzling since the *s* and the *r* processes require neutron densities that are more than ten orders of magnitude apart, and hence are thought to occur in very different stellar sites with very different physical conditions. We investigate whether the abundance patterns of CEMP-*s/r* stars can arise from the nucleosynthesis of the intermediate neutron-capture process (the *i* process), which is characterised by neutron densities between those of the *s* and the *r* processes. Using nuclear network calculations, we study neutron capture nucleosynthesis at different constant neutron densities  $n$  ranging from  $10^7$  to  $10^{15}$  cm<sup>-3</sup>. With respect to the classical *s* process resulting from neutron densities on the lowest side of this range, neutron densities on the highest side result in abundance patterns that show an increased production of heavy *s*-process and *r*-process elements but similar abundances of the light *s*-process elements. Such high values of  $n$  may occur in the thermal pulses of asymptotic giant branch (AGB) stars due to proton ingestion episodes. Comparison to the surface abundances of 20 CEMP-*s/r* stars show that our modelled *i*-process abundances successfully reproduce observed abundance patterns that could not be previously explained by *s*-process nucleosynthesis. Because the *i*-process models fit the abundances of CEMP-*s/r* stars so well, we propose that this class should be renamed as CEMP-*i*.

*Subject headings:* nuclear reactions, nucleosynthesis, abundances, stars: chemically peculiar, stars: carbon, stars: AGB and post-AGB, binaries: general

## 1. INTRODUCTION

In the Galactic Halo we can find metal-poor ( $[\text{Fe}/\text{H}] < -1$ ) and very metal-poor ( $[\text{Fe}/\text{H}] < -2$ ) stars which are amongst the oldest stars that we observe. They have formed from almost primordial material that contains the signatures of the first nucleosynthesis and chemical enrichment events in the Universe. Multiple surveys providing chemical abundances for these low-mass, barely evolved objects have revealed a large fraction of carbon-enhanced metal-poor (CEMP) stars (e.g. Frebel et al. 2006; Lucatello et al. 2006; Lee et al. 2013; Yong et al. 2013; Placco et al. 2014). These are generally defined by a carbon excess<sup>7</sup> of  $[\text{C}/\text{Fe}] > 1$ . CEMP stars are subdivided into four classes based on their content of the heavy elements barium and europium, which are produced by the slow (*s*) and the rapid (*r*) neutron-capture process, respectively. The exact definitions vary amongst authors (e.g. Beers & Christlieb 2005; Jonsell et al. 2006;

Masseron et al. 2010; Lugaro et al. 2012) and the categories adopted in this work are:

- **CEMP-s** stars show enhancement of barium. This class is defined by  $[\text{Ba}/\text{Fe}] > 1$ ,  $[\text{Ba}/\text{Eu}] > 0$  and  $[\text{Eu}/\text{Fe}] \leq 1$  and consequently is thought to show *s*-process enrichment only.
- **CEMP-s/r** stars also show barium enhancement, as defined for CEMP-s stars with  $[\text{Ba}/\text{Fe}] > 1$  and  $[\text{Ba}/\text{Eu}] > 0$ , but are additionally enriched in europium with  $[\text{Eu}/\text{Fe}] > 1$ .
- **CEMP-r** stars are enriched in *r*-process elements, in particular in europium compared to iron and barium:  $[\text{Eu}/\text{Fe}] > 1$  and  $[\text{Ba}/\text{Eu}] < 0$ . Only a few CEMP stars are currently known to fall into this category (Snedden et al. 2003a; Hansen et al. 2015).
- **CEMP-no** stars show no particular enhancements in heavy elements (Aoki et al. 2002b).

The variety of heavy-element abundance patterns observed in CEMP stars points to different formation scenarios, in particular due to the differences in the production of *s*- and *r*-process elements. The low neutron densities which are required to meet the conditions for the *s* process are approximately  $n \approx 10^6$  cm<sup>-3</sup> to  $10^{10}$  cm<sup>-3</sup> (Busso et al. 1999) and result in a neutron capture path which runs close to the valley of stability. The predominant producer of *s*-process elements are asymptotic giant branch (AGB) stars (e.g., Gallino et al. 1998; Karakas & Lattanzio 2014). On the other hand, the *r* process is characterised by neutron densities higher than

mhampel@lsw.uni-heidelberg.de

<sup>1</sup>Zentrum für Astronomie der Universität Heidelberg, Landessternwarte, Königstuhl 12, 69117 Heidelberg, Germany

<sup>2</sup>Argelander-Institut für Astronomie, University of Bonn, Auf dem Hügel 71, 53121 Bonn, Germany

<sup>3</sup>Konkoly Observatory, Research Centre for Astronomy and Earth Sciences, Hungarian Academy of Sciences, H-1121 Budapest, Hungary

<sup>4</sup>Monash Centre for Astrophysics, Monash University, VIC3800, Australia

<sup>5</sup>Department of Physics and Astronomy, Clemson University, Clemson, SC, 29634-0978, USA

<sup>6</sup> $[\text{A}/\text{B}] = \log_{10}(N_{\text{A}}/N_{\text{B}})_{*} - \log_{10}(N_{\text{A}}/N_{\text{B}})_{\odot}$ , with the number densities  $N_{\text{A}}$ ,  $N_{\text{B}}$  of element A and B, respectively, where the indices \* and  $\odot$  denote the stellar and the solar values.

<sup>7</sup>Different authors have adopted other definitions of CEMP stars using  $[\text{C}/\text{Fe}] > 0.5$  or  $[\text{C}/\text{Fe}] > 0.7$  (e.g. Aoki et al. 2007).

$\simeq 10^{20} \text{ cm}^{-3}$ . Because the  $r$  process requires extreme conditions, it is believed to occur during supernovae explosions and/or neutron star mergers (Thielemann et al. 2011; Wehmeyer et al. 2015).

The carbon enhancement of CEMP-no and CEMP- $r$  stars is believed to originate from pre-enhancement of the interstellar medium from which these stars formed (e.g. Cooke & Madau 2014; Frebel & Norris 2015, and references therein). This is supported by observations of very metal-poor damped-Lyman  $\alpha$  absorption systems that show enrichment in carbon (Cooke et al. 2011). These categories of CEMP stars are not discussed further in this work.

The widely accepted origin for the enrichments of carbon and  $s$ -process elements in CEMP- $s$  stars is accretion of matter from an AGB companion in a binary system. Carbon and  $s$ -process elements are known products of AGB nucleosynthesis (e.g., Karakas & Lattanzio 2014) and studies of radial velocity variations in CEMP- $s$  stars are consistent with all CEMP- $s$  stars being in binaries<sup>8</sup> (Lucatello et al. 2005; Starkenburg et al. 2014). However, this formation scenario cannot explain the origin of CEMP- $s/r$  stars because current AGB models do not produce enough barium, let alone enough europium (Lugaro et al. 2012). Given that we believe that the  $s$  and the  $r$  processes occur in completely different sites under completely different conditions, it is puzzling how these stars exhibit signatures of both processes. Various formation scenarios have been considered (Jonsell et al. 2006; Lugaro et al. 2009) where the  $s$ -process enrichment originates from pollution from an AGB companion, similarly to the formation scenario for CEMP- $s$  stars. In this framework, the additional enrichment in  $r$ -process elements has been ascribed to:

- a primordial origin, due to pollution of the birth cloud of the binary system by an  $r$ -process source (Bisterzo et al. 2011)

or to result from the ejecta of the explosion of

- a third, massive star in a triple system (Cohen et al. 2003)
- or the primary itself
  - either as a type 1.5 supernova (Zijlstra 2004; Wanaajo et al. 2006)
  - or due to an accretion induced collapse (Qian & Wasserburg 2003; Cohen et al. 2003).

Abate et al. (2016) show that these formation scenarios have significant difficulties in explaining the observed number of CEMP- $s/r$  stars, in particular in comparison to the number of CEMP- $s$  and CEMP- $r$  stars. Additionally, the observed correlation between the enrichment in  $s$ - and  $r$ -process elements in CEMP- $s/r$  stars, as well as high observational ratios of heavy  $s$ -process elements (hs) to light  $s$ -process elements (ls) provide a challenge (e.g. Lugaro et al. 2012; Abate et al. 2015a, 2016).

As it is difficult to explain the  $s/r$  abundance pattern via pollution from two independent stellar sites, one

<sup>8</sup> Hansen et al. (2016) have called this into question. However, the binary star fraction for CEMP- $s$  stars is still significantly higher than for other metal-poor stars.

may wonder whether it is possible to form both  $s$ - and  $r$ -process elements at *the same* site through the action of a modified neutron-capture process operating at neutron densities in between the  $s$  and  $r$  process: the intermediate neutron-capture process (the  $i$  process) with densities of the order of  $n \approx 10^{15} \text{ cm}^{-3}$  (Cowan & Rose 1977). Compared to the  $s$  process, this neutron-capture process should be able to account for both an increased production of  $r$ -process elements as well as a higher hs-to-ls ratio. Initial attempts to explain the abundances of three CEMP- $s/r$  stars by the  $i$  process have been made by Dardelet et al. (2014).

For the  $i$  process to occur, a neutron burst is required which is significantly different from that occurring in AGB stars responsible for the  $s$  process. There are peculiarities in the evolution of low-metallicity AGB stars that may allow this to happen. In AGB stars with low CNO content, the intershell convection zone that develops during a thermal pulse is able to penetrate up into the hydrogen burning shell, drawing protons down into hot regions (e.g. Fujimoto et al. 2000; Campbell & Lattanzio 2008; Lau et al. 2009). These protons are able to react with the abundant  $^{12}\text{C}$  present in the intershell to form  $^{13}\text{C}$ , which acts as a neutron source via the  $^{13}\text{C}(\alpha, n)^{16}\text{O}$  reaction. These so-called proton ingestion episodes (PIEs) may result in high neutron densities, up to the requisite  $n = 10^{15} \text{ cm}^{-3}$  (Cristallo et al. 2009). A PIE can also develop during the core helium flash (e.g. Fujimoto et al. 1990; Lugaro et al. 2009) with similar consequences for nucleosynthesis (Campbell et al. 2010). More recently, calculations by Jones et al. (2016) suggest that PIEs can also take place in the most massive AGB stars, the super AGB stars (see also Doherty et al. 2015). Unfortunately, the quantitative predictions of all these 1D stellar evolution calculations are severely limited by the simplistic treatment of convection used in these codes. Hydrodynamical simulations of proton ingestion (Herwig et al. 2011; Stancliffe et al. 2011; Herwig et al. 2014; Woodward et al. 2015) show complex behaviour, the outcome of which is still a matter of debate.

Motivated by the puzzling abundance patterns of CEMP- $s/r$  stars and the question of whether a single process can explain the signatures of both the  $s$  and  $r$  process, this study investigates the nucleosynthesis of the intermediate ( $i$ ) process. We present single zone nuclear network calculations under conditions representative of the intershell region of a low-mass, low-metallicity AGB star and examine neutron-capture processes at different constant neutron densities, to determine whether the abundance patterns in CEMP- $s/r$  stars can be obtained.

## 2. METHOD

The nucleosynthesis tools that we use are *NucNet Tools*, a set of C/C++ codes developed by Meyer (2012). *NucNet Tools* can be used to create nuclear-reaction networks and model the formation of elements in stars, supernovae, and related environments. In this study, the codes are used to follow the nuclear processing of a single zone with given initial composition under conditions of fixed temperature and density. One can also specify a species whose abundance should be kept constant throughout the calculations, which can be used, for example, to artificially induce neutron-capture nucleosyn-

thesis (as we do here) or to imitate a mixing process that maintains a constant level of a certain species by mixing in material.

The nuclear network used for this project contains the 5442 isotopes and 45831 reactions from the JINA Reaclib V0.5 database (Cyburt et al. 2010). In more recent releases, neutron-capture reaction rates from KADoNiS v0.2 (Dillmann et al. 2006) are included and refitted to eliminate blow-ups at low temperatures and to match the theory at higher temperatures (JINA Reaclib label *kd02*). However, in some cases the fits underpredict the rates in the temperature regime relevant for the conditions in an AGB intershell region, with deviations up to two orders of magnitude, for example, in the case of  $^{151}\text{Eu}(n,\gamma)^{152}\text{Eu}$ . Such a large underprediction of the reaction rate introduces artificial bottlenecks on the neutron capture path. Because of this, we use the previous version of the refitted rates (JINA Reaclib label *ka02*). Twenty-eight  $\alpha$ -decay rates (Tuli 2011), which are important for the *s*-process and its termination because of being close to the valley of stability, were selected and added to the network. These decay rates are listed in the online-only Table 3.

The physical input conditions are adapted from the density and temperature profiles of the intershell region that Stancliffe et al. (2011) found for a low-metallicity AGB star. In particular, we present here the test case with  $T = 1.5 \times 10^8$  K and  $\rho = 1600$  g cm $^{-3}$ . Different temperatures and densities in the range of  $1.0 \times 10^8$  K  $\leq T \leq 2.2 \times 10^8$  K and  $800$  g cm $^{-3} \leq \rho \leq 3200$  g cm $^{-3}$  were also tested without significant changes in the results.

To model the nucleosynthesis in the intershell region, the composition of the input zone is adapted from the intershell composition of Abate et al. (2015b, and references therein). In particular, we use the abundances of 320 isotopes from an AGB star model with metallicity  $Z = 10^{-4}$  and initial mass  $M = 1 M_{\odot}$  after the second thermal pulse.

At  $n = 10^{15}$  cm $^{-3}$  the evolution of the abundance distribution is then followed for  $t = 0.1$  yr, which results in a neutron exposure of  $\tau = 495$  mb $^{-1}$ . The run times of the models at lower neutron densities are scaled with  $n$  to ensure the same neutron exposure. Such a large value ensures that the resulting abundance pattern represents the equilibrium abundance pattern between the heavy elements and the seed nuclei. Once this equilibrium is reached, the element-to-element ratio is a function of the constant neutron density and is not altered by further neutron exposure at the same neutron density. In other words, the abundance pattern is independent of the actual neutron exposure, as long as equilibrium is reached. We note that it is still uncertain what typical neutron exposures are expected from proton ingestion episodes in AGB stars and that realistic values are therefore unknown. To match abundance patterns of CEMP-*s/r* stars with *i*-process nucleosynthesis, Dardelet et al. (2014) found neutron exposures that are about an order of magnitude lower than we assume. However, reducing the neutron exposure by one order of magnitude has a negligible effect on the abundance patterns studied in this work as the heavy elements are already close to equilibrium with one-another: for example, the relative abundance of barium and europium [Ba/Eu] varies by less than 1% during this period. The limitation of

studying equilibrium abundance patterns is that it is not possible to predict abundances at the termination point of the neutron capture path at the lead peak. While the element-to-element ratios of the other heavy elements do not change with further neutron exposure, the lead-peak elements are only produced and not destroyed by neutron capture processes and can therefore not reach an equilibrium. This makes the lead abundance sensitive to the final neutron exposure. Adding the total neutron exposure as a degree of freedom should therefore be considered in future work to further constrain the *i* process. Subsequent to the exposure to the constant neutron density, the neutron flux is turned off and the successive decays are followed for  $t = 10$  Myr to allow the long-lived unstable isotopes to decay.

Finally, while we keep the neutron density constant over the whole time interval and switch the neutron source off instantaneously, a more realistic profile would show the neutron density decrease with time. We tested this behaviour by including a smoother decrease and found that the final abundances are similar to those presented here only if the decrease is relatively fast with the time scale depending on the neutron density. For  $n = 10^{12}$  cm $^{-3}$  the decrease can last for about a year before any changes are seen in the final abundances, while for  $n = 10^{15}$  cm $^{-3}$  the decrease has to be extremely fast, of the order of a few hours, to keep the same results as presented here. This effect needs to be further investigated in the future.

### 3. RESULTS AND DISCUSSION

When exposed to free neutrons, the present seed nuclei, in particular the abundant iron peak nuclei, repeatedly undergo neutron capture reactions. Due to the  $\beta$ -decays of unstable, neutron-rich isotopes, heavy elements are created. Fig. 1 compares the neutron-capture paths in a section of the nuclide chart for the two different neutron densities of  $n = 10^7$  cm $^{-3}$  and  $n = 10^{15}$  cm $^{-3}$ . A higher neutron density creates a neutron capture path further away from the valley of stability because an unstable nucleus can form an even heavier isotope by neutron capture instead of decaying. Thereby different equilibrium abundance ratios between the isotopes are reached that are characteristic for each neutron density. The final heavy-element abundances, i.e. after the decays of unstable nuclei, for the simulations with different neutron densities are listed in detail in the online-only Table 4.

Fig. 2 shows the characteristic equilibrium pattern of a neutron source active at  $n = 10^{15}$  cm $^{-3}$  prior to the  $\beta$  decays, as well as the final heavy-element abundance pattern when unstable nuclei have decayed after the neutron source is switched off. For comparison, the resulting abundance pattern of the simulation with a neutron density of  $n = 10^7$  cm $^{-3}$  is also shown.

For the low neutron density a typical *s*-process abundance pattern arises with characteristic elements that are stable bottleneck nuclei with magic neutron numbers. These form the light *s*-process (ls) peak (e.g. Sr, Y, and Zr with atomic numbers  $Z = 38, 39,$  and  $40,$  respectively), the heavy *s*-process (hs) peak (e.g. Ba, La, Ce with atomic numbers  $Z = 56, 57,$  and  $58,$  respectively), and the lead peak ( $Z = 82$ ).

With the active source at  $n = 10^{15}$  cm $^{-3}$ , the equilibrium abundance pattern shows a shift of the ls and hs

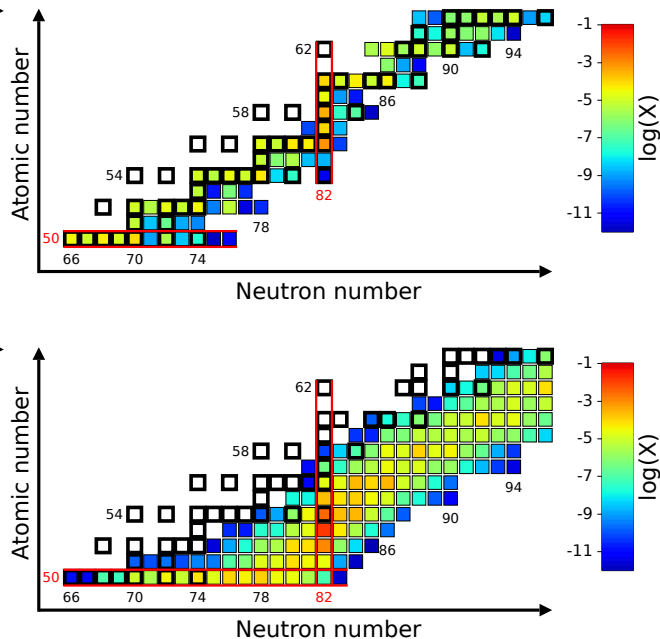


FIG. 1.— Neutron capture paths of the models with a constant neutron density of  $n = 10^7 \text{ cm}^{-3}$  (upper panel) and  $n = 10^{15} \text{ cm}^{-3}$  (lower panel) shown in the section of the nuclide chart including isotopes of the elements from tin to gadolinium. Isotopes are located as a function of their neutron and proton number and stable isotopes are highlighted by bold black borders. The magic proton and neutron numbers are framed in red. The colours represent the mass fraction of each isotope and thereby show where the neutron capture path produces heavy elements. For  $n = 10^7 \text{ cm}^{-3}$  the paths runs mainly through the stable isotopes and stays close to the valley of stability. For  $n = 10^{15} \text{ cm}^{-3}$  the paths runs much further away on the neutron rich side from the valley of stability. Note the pile-up at  $^{135}\text{I}$  with magic neutron number 82 for  $n = 10^{15} \text{ cm}^{-3}$ .

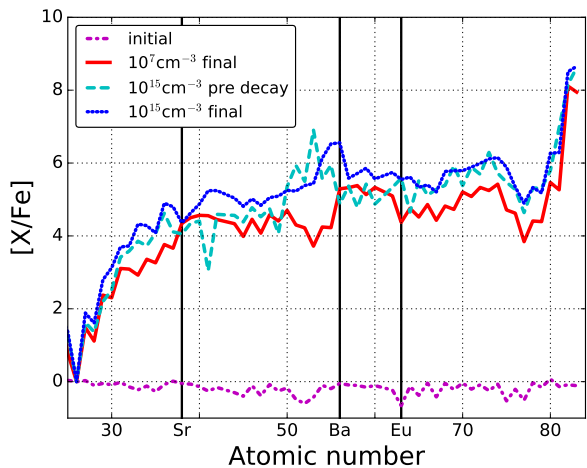


FIG. 2.— Abundance distributions of the two simulations with neutron densities of  $n = 10^7 \text{ cm}^{-3}$  and  $n = 10^{15} \text{ cm}^{-3}$ . For  $n = 10^7 \text{ cm}^{-3}$  the pattern created by the active neutron source is sufficiently similar to the final distribution (red line). On the other hand, the nuclei created by the active source with  $n = 10^{15} \text{ cm}^{-3}$  are mainly unstable which results in the need to differentiate between the characteristic abundance pattern when the source is active (cyan dashed line) and the final distribution after decays when the source has been switched off (blue dotted line). The initial distribution is shown by the magenta dot-dashed line. The vertical lines show the location of Sr, Ba and Eu which are representatives of the light *s*- and heavy *s*-process peak as well as the *r* process, respectively.

peaks to lighter elements, mainly dominated by a peak at iodine. This is caused by the shift of the neutron capture path that encounters isotopes with magic neutron numbers at lower atomic numbers compared to the *s* process (compare the panels of Fig. 1). In particular, the magic, but unstable, isotope  $^{135}\text{I}$  ( $Z = 53$ ) acts as the bottleneck of the neutron capture path at  $n = 10^{15} \text{ cm}^{-3}$ . The final abundance pattern of the *i* process shows a peak at barium due to the decays of the abundant  $^{135}\text{I}$  into stable  $^{135}\text{Ba}$ .

The comparison of the final abundance patterns of  $n = 10^7 \text{ cm}^{-3}$  and  $n = 10^{15} \text{ cm}^{-3}$  shows that the abundance of strontium, a representative of the *ls* peak, does not change. The final abundances of barium and europium, representatives of the *hs* peak and the *r* process respectively, both increase with neutron density. This makes processes at higher neutron densities promising candidates to explain the discrepancies found between the CEMP-*s/r* surface abundances and abundance patterns modelled with AGB nucleosynthesis simulations by e.g. Abate et al. (2015a); Lugaro et al. (2012); Bisterzo et al. (2012).

Furthermore, the distribution of the abundances within the *ls* and *hs* peaks is strongly modified: in the case of the *s* process, Sr, Y, and Zr are inevitably overproduced by the same amount, and the same applies to Ba, La, and Ce. On the other hand, in the case of the *i* process, there is an increase of around a factor of 3 between the production of Sr and that of Zr; and a factor of 10 decrease between Ba and La and/or Ce. In fact, the overproduction of Ba with respect to La resulting from the *i* process has been pointed out as the possible source of the Ba excess observed in open clusters (Mishenina et al. 2015).

### 3.1. Comparison to CEMP-*s/r* stars

The abundances of 67 CEMP stars with barium enhancement were studied by Abate et al. (2015a), 20 of which are classified as CEMP-*s/r* stars. This sample of CEMP-*s/r* stars is based on the SAGA database (Suda et al. 2008). The objects and their properties are listed in Table 5 and were selected in the metallicity range  $-2.8 \leq [\text{Fe}/\text{H}] \leq -1.8$ . For further information regarding the data sample see Abate et al. (2015a)<sup>9</sup>. As Abate et al. (2015a) were unable to obtain satisfactory fits to these 20 stars using standard *s*-process calculations, we shall compare the final abundance patterns of our *i*-process calculations with neutron densities of  $n = 10^{12}$ ,  $10^{13}$ ,  $10^{14}$ , and  $10^{15} \text{ cm}^{-3}$  to these objects to see if we can obtain better fits.

To compare the model abundances to the surface abundances of the CEMP-*s/r* stars, we need to mix an unknown quantity of *i*-processed material with non-processed material. Some mixing will occur because dredge-up must presumably extract the *i*-processed material from the stellar interior to its envelope. As we assume that CEMP-*s/r* stars form in a similar manner to CEMP-*s* stars (i.e. from mass transfer in binary systems), further dilution can also occur once this material is transferred to its companion (Stancliffe et al. 2007,

<sup>9</sup> For HE1305+007 information on Zr is available from Goswami et al. (2006). We add  $[\text{Zr}/\text{Fe}] = 2.09 \pm 0.3$  to the data used by Abate et al. (2015a).

2013). We therefore assume that the convective envelope and the secondary star both have initially Solar element-to-element ratios for the heavy elements, although it should be kept in mind that this initial relative composition could have been different from Solar, and closer to that of pristine Galactic material, such as observed in CEMP-no stars. In any case, because these stars do not show enhancements in elements heavier than iron, the final resulting pattern would not be greatly affected. The modelled surface abundances of the CEMP- $s/r$  star can then be computed using the following equation:

$$X = X_i \times (1 - d) + X_{\odot} \times d,$$

where  $X$  is the final abundance,  $X_i$  the abundance from the modelled  $i$  process after the decays,  $X_{\odot}$  the solar-scaled abundance and  $d$  a dilution factor. The dilution factor is a free parameter in these simulations and is varied in order to find the best fitting model to the observational data for each simulation with a different constant neutron density. In order to find the best fitting model  $\chi^2$  is computed for each simulation from:

$$\chi^2 = \sum_Z \frac{([X_Z/\text{Fe}]_{\text{obs}} - [X_Z/\text{Fe}]_{\text{mod}})^2}{\sigma_{Z,\text{obs}}^2},$$

where  $[X_Z/\text{Fe}]_{\text{obs}}$  and  $[X_Z/\text{Fe}]_{\text{mod}}$  are the observed and modelled abundances, respectively, of the element with atomic number  $Z$  and  $\sigma_{Z,\text{obs}}$  is the observational error of  $[X_Z/\text{Fe}]_{\text{obs}}$ . For these calculation, the abundances of the heavy elements with  $30 < Z \leq 80$  were taken into account. The abundances of elements with  $Z \leq 30$  are not significantly produced in the studied neutron-capture processes and are therefore not considered. We explicitly exclude Pb from the computation, because the final Pb abundance depends on the actual neutron exposure. For all the other elements, once equilibrium is achieved during neutron exposure, the abundance ratios will not change. To quantify the deviations between the predictions of the best-fitting model and the observed abundances, the residual is defined as

$$R_Z = [X_Z/\text{Fe}]_{\text{obs}} - [X_Z/\text{Fe}]_{\text{mod}}. \quad (1)$$

The following example fit shows the influence of the two degrees of freedom in the fits, namely the dilution factor,  $d$ , and the neutron density,  $n$ . Fig. 3 shows the abundance pattern of the CEMP- $s/r$  star LP625-44 and the best fitting model with a neutron density of  $n = 10^{14} \text{ cm}^{-3}$  and a dilution factor  $d = 0.917$ . For comparison, two alternative models with a higher and a lower dilution factor at the same neutron density are shown. The higher the dilution factor, the lower are the abundances of heavy elements. Therefore the main influence of the dilution factor is to set the right abundance level to match that of the CEMP- $s/r$  star. Table 1 lists the best-fitting dilution factors for each of the tested neutron densities along with the minimal  $\chi^2$  for each  $n$ . While  $d$  predominantly determines the overall abundance level, the variation of  $n$  has a higher impact on the individual element-to-element ratios and hence influences the quality of the fit indicated by the value of  $\chi^2$ . We note that for some systems (e.g., LP625-44), the reduced  $\chi^2$  is less than 1. While this could be interpreted as suggesting the error bars are too large, one should not rely on the statistical quantitative meaning of  $\chi^2$  because the errors on

abundance measurements are not simply Gaussian measurement errors. Therefore  $\chi^2$  is just an indicator to identify which model matches the observations best, but its value does not have the statistical meaning in the usual sense.

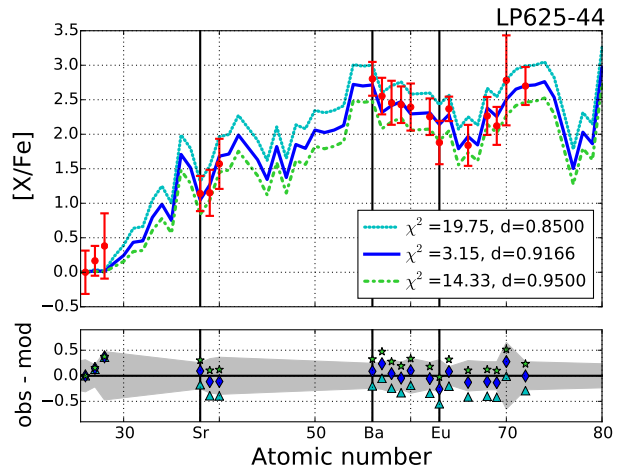


FIG. 3.— Influence of the dilution factor on the modelled abundances of CEMP- $s/r$  star LP625-44. The observed surface abundances (red dots) and the best-fitting model at  $n = 10^{14} \text{ cm}^{-3}$  with a dilution factor of  $d = 0.917$  (blue) are compared to the abundance distributions with two alternative dilution factors of  $d = 0.850$  (cyan) and  $d = 0.950$  (green). The lower panel shows the distribution of the residuals as defined in Equation 1. The uncertainty of the observations  $\sigma_{Z,\text{obs}}$  is indicated by errorbars in the upper panel and by the shaded region in the lower panel. The vertical lines show the location of Sr, Ba and Eu which are representatives of the ls and hs peak as well as the  $r$  process, respectively.

TABLE 1  
FIT PARAMETERS FOR THE CEMP- $s/r$  STAR LP625-44. THE BEST-FITTING MODEL IS THE ONE WITH  $n = 10^{14} \text{ cm}^{-3}$ , AS INDICATED BY A CLEAR MINIMUM IN  $\chi^2$ .

$n \text{ (cm}^{-3}\text{)}$	$d$	$\chi^2$
$10^{12}$	0.932	8.2
$10^{13}$	0.933	6.4
$10^{14}$	0.917	3.2
$10^{15}$	0.862	8.7

The details of the best-fitting model for all 20 stars, i.e., how many measurements the fit is based on, the neutron density of the model, dilution factor and  $\chi^2_{\text{min}}$  of the best fit, are listed in Table 2. For most of the stars the majority of the elemental abundances can be reproduced within the uncertainty of the observational measurements. One significant exception is SDSSJ0912+0216 which has an unusual abundance pattern that is unlike the other stars in the sample. It cannot be reproduced by either an  $i$  or  $s$  process. Further study of this object is warranted. Two stars, BS16080-175 and BS17436-058, only have measurements of heavy elements for barium, lanthanum and europium that the fit can be based on. Due to this low number of observations, their fits are less meaningful than for the remaining stars with significantly more observed abundances. Interestingly, most of the abundance patterns of the remaining 17 stars can be best modelled by a neutron capture process operating at a neutron density of  $n = 10^{14} \text{ cm}^{-3}$ , which is



the case for 12 stars. Four stars are better described by processes operating at the lower neutron densities of  $n = 10^{12} \text{ cm}^{-3}$  (CS22881-036 and HD187861) and  $n = 10^{13} \text{ cm}^{-3}$  (CS22948-027 and HD224959). The only star for which the best fit to the data is achieved by the model of the  $i$  process operating at a neutron density of  $n = 10^{15} \text{ cm}^{-3}$  is CS31062-050. However, the abundances of CS31062-050 can be modelled almost as well by the simulation of  $n = 10^{14} \text{ cm}^{-3}$  with  $\chi^2 = 26.7$  compared to  $\chi^2 = 26.5$  for  $n = 10^{15} \text{ cm}^{-3}$ . Therefore it is arguable that a neutron density around  $n = 10^{14} \text{ cm}^{-3}$  is sufficient to reproduce the abundance patterns of most CEMP- $s/r$  stars, because this is the case that results in both high Eu abundances and  $[\text{Ba}/\text{Eu}] \approx 0.6$  as observed in CEMP- $s/r$  stars.

### 3.2. Comparison to other studies

While the original idea for the  $i$  process is not new (Cowan & Rose 1977), there have been few studies of its production of the heavy elements to which we can compare our results. In the context of CEMP- $s/r$  stars, Dardelet et al. (2014) examined its effects on three CEMP- $s/r$  stars: CS22898-027, CS31062-050, HE0338-3945. Like our simulations, these authors used a single-zone nucleosynthesis code to compute the effects of the  $i$  process but rather than using a constant neutron density, they adopt a constant combined C+H mass fraction of 0.7 to simulate proton ingestion. For the three systems they studied they found similar fitting neutron densities to those we have obtained and essentially the same resulting abundance pattern.

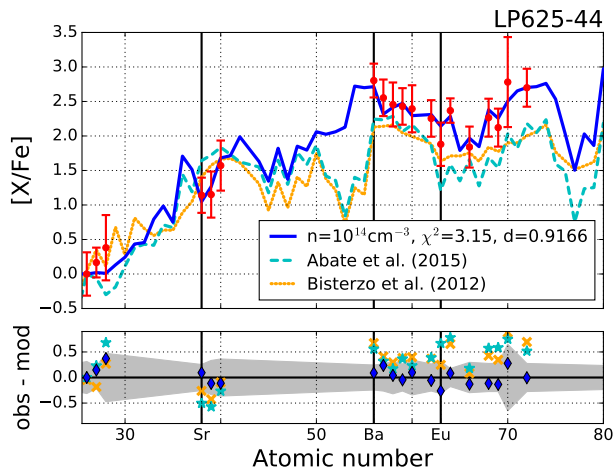


FIG. 4.— Best fitting model for CEMP- $s/r$  star LP625-44 (red dots): the best-fitting models from Abate et al. (2015a) with AGB nucleosynthesis (cyan) and from Bisterzo et al. (2012) with  $s$ -process and initial  $[\text{r}/\text{Fe}]=1.5$  (orange) compared to the best-fitting model from the neutron capture nucleosynthesis calculations with a neutron density of  $n = 10^{14} \text{ cm}^{-3}$  (blue). Lower panel, vertical lines and uncertainties as in Fig. 3.

Fig. 4 shows the observed abundance pattern of LP625-44 and the best-fitting model from this work, along with the best fitting model from the studies of Abate et al. (2015a) and Bisterzo et al. (2012). It can be seen that the main problems of the fit with standard AGB nucleosynthesis - to explain the high  $[\text{hs}/\text{ls}]$  ratio as well as the high Eu ( $Z = 63$ ) abundance - are almost entirely resolved by modelling the CEMP- $s/r$  sur-

face abundances with  $i$ -process neutron-capture nucleosynthesis with  $n = 10^{14} \text{ cm}^{-3}$ . Best fit  $s$ -process models present further problems in reproducing the abundances of the elements between Eu and Hf ( $Z = 72$ ) and relative abundance variations within the first and second  $s$ -process peaks, where Zr and Ba are often observed to be higher than Sr-Y and La-Ce, respectively.

Because of these problems, Bisterzo et al. (2012) considered diluting  $s$ -processes material not with pristine material, but with matter that was pre-enriched in  $r$ -process elements. Diluting  $s$ -process material presents similar problems to those described above, even when the initial  $r$ -process abundances are assumed to be enhanced by  $[\text{r}/\text{Fe}]=1-2$  dex in order to match the  $[\text{Eu}/\text{Fe}]$  abundance (see, e.g., the best fit for LP625-44 in Fig. 31 of Bisterzo et al. (2012)). Patterns which match much better are instead found in our  $i$ -process results.

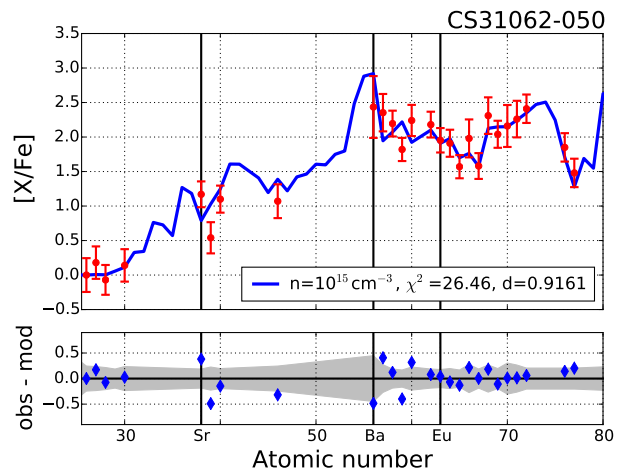


FIG. 5.— Best fitting  $i$ -process model for CEMP- $s/r$  star CS31062-050 (red dots). The  $s$ -process best fit with initial  $[\text{r}/\text{Fe}]=1.6$  can be found in Fig. 26 of Bisterzo et al. (2012).

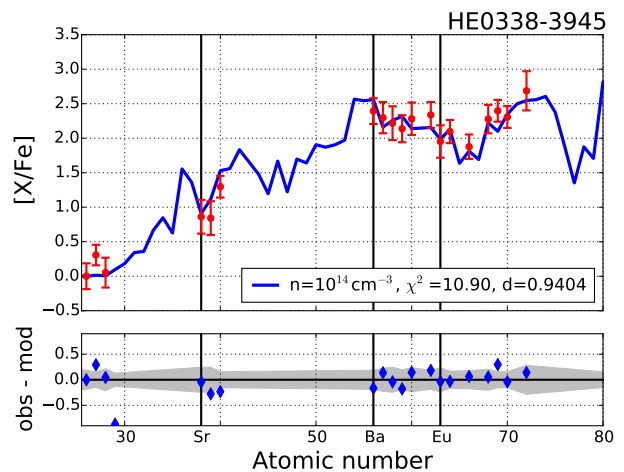


FIG. 6.— Best fitting  $i$ -process model for CEMP- $s/r$  star HE0338-3945 (red dots). The  $s$ -process best fit with initial  $[\text{r}/\text{Fe}]=2$  can be found in Fig. 19 of Bisterzo et al. (2012).

In Figs. 5 to 7, we show further examples of our  $i$ -process fits and the captions provide references to the fits of Bisterzo et al. (2012) for comparison. Our remaining

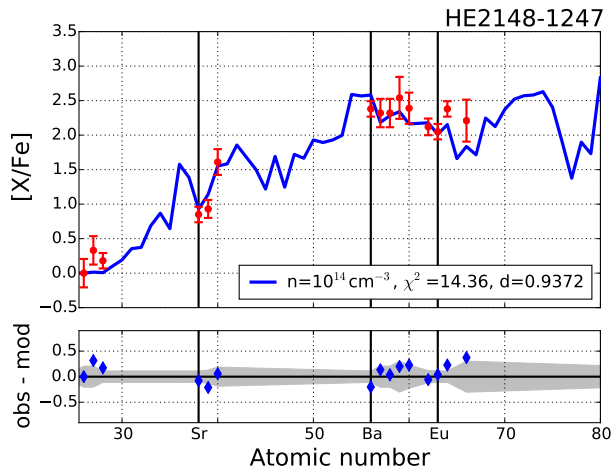


FIG. 7.— Best fitting *i*-process model for CEMP-*s/r* star HE2148-1247 (red dots). The *s*-process best fit with initial  $[r/Fe]=2$  can be found in Fig. 21 of Bisterzo et al. (2012).

individual fits can be found in Appendix C. The stars presented in Figs. 4 to 7 have the largest number of observed elements (between 25 and 37), providing the most stringent test bed for our model. Detailed inspection of these figures demonstrates that there is an excellent match between our models and the observations, superior to any *s*-process fits presented so far. Furthermore, the match not only involves the abundance of Eu, but also several other relatively minor details that have been problematic for the *s*-process models: the relative abundances of Sr, Y, Zr and of Ba, La, and Ce; the elements between Eu and Hf; the abundance of Pd ( $Z = 46$ ), as discussed below. For example, a clearly better match with the abundances of the elements between Eu and Hf is shown by LP625-44 (Fig. 4) and CS31062-050 (Fig. 5). A match with the observed positive  $[Ba/La]$  and  $[Ba/Ce]$  ratios is shown by LP625-44 (Fig. 4), CS31062-050 (Fig. 5) and HE0338-3945 (Fig. 6). It is also possible to obtain a better match with the abundance pattern of the first *s*-process peak as shown by all the plotted individual fits, although in most cases (for example CS31062-050, Fig. 5) it appears that a shift of the local abundance minimum from Sr to Y would provide a better match. This issue may be related to nuclear uncertainties in the production of the first peak. Finally, the best *s*-process fits for CS31062-050 show an overabundance of Pd, which required Bisterzo et al. (2012) to assume a further “light-element *r*-process enhancement” of 0.5 dex for the elements from Mo ( $Z = 42$ ) to Cs ( $Z = 55$ ). The *i* process on the other hand naturally explains an increase in Pd (Fig. 5), even to an extent that slightly overpredicts the measurement.

Fig. 8 shows the residuals of every observed element for each star and their average. As a comparison, the average value of the residuals from Abate et al. (2015a) is shown as well. The majority of the averaged residuals from this work lie within the observational uncertainty of the measurements. This result was not achieved previously when standard AGB nucleosynthesis only was used to model the surface abundances of CEMP-*s/r* stars (Abate et al. 2015a).

For the heavy elements considered in the fits, only the average residual for Y lies on the boundary of the average measurement uncertainty, while the single Pd measure-

TABLE 2  
FIT PARAMETERS FOR EACH CEMP-*s/r* STAR: NUMBER OF MEASUREMENTS THE FIT IS BASED ON, NEUTRON DENSITY  $n$ , DILUTION FACTOR  $d$  AND MINIMUM  $\chi^2$ .

ID	$N_{\text{obs}}$ ( $31 \leq Z \leq 80$ )	$\log(n/\text{cm}^{-3})$	$d$	$\chi^2_{\text{min}}$
BS16080-175	3	12	0.991	2.0
BS17436-058	3	13	0.989	0.2
CS22881-036	7	12	0.985	5.1
CS22898-027	11	14	0.937	5.7
CS22948-027	9	13	0.965	5.9
CS29497-030	15	14	0.957	8.1
CS29526-110	7	14	0.966	2.7
CS31062-012	7	14	0.971	3.2
CS31062-050	22	15	0.916	26.5
HD187861	8	12	0.978	0.5
HD224959	8	13	0.969	3.7
HE0131-3953	6	14	0.969	0.4
HE0143-0441	8	14	0.947	9.0
HE0338-3945	16	14	0.940	10.9
HE1105+0027	6	14	0.953	1.2
HE1305+0007	10	14	0.858	7.6
HE2148-1247	12	14	0.937	14.4
HE2258-6358	17	14	0.973	23.4
LP625-44	16	14	0.917	3.2
SDSSJ0912+0216	16	14	0.938	373.7

ment is overpredicted in the corresponding best-fitting model to an extent only slightly outside the observational error. The remaining observed abundances of 21 elements with  $30 < Z \leq 80$  are reproduced by the models of neutron capture nucleosynthesis with neutron densities in the *i*-process regime within the accuracy limited by the average errors in the measurements. We therefore believe the *i* process is a valid component of the formation scenario of CEMP-*s/r* stars. In particular, the possible connection of *i*-process nucleosynthesis and PIEs in low-metallicity AGB stars suggest a good candidate for a formation scenario of CEMP-*s/r* stars in a binary system, analogous to the formation of CEMP-*s* stars. This is supported by radial velocity measurements of CEMP-*s/r* stars (Hansen et al. 2016; Lucatello et al. 2009). However, in this formation scenario it is likely that an AGB star with PIEs and *i*-process nucleosynthesis also undergoes “normal” thermal pulses with *s*-process nucleosynthesis. This means that the resulting heavy-element abundance pattern is most likely a superposition of an *s*- and *i*-process abundance pattern, instead of the pure *i*-process pattern studied in this work. An example of this might be the case of HE2148-1247 where the *i* process underestimates the Gd ( $Z = 64$ ) and Dy ( $Z = 66$ ) abundances (Fig. 7). In this case, dilution of the *i*-processed matter with *s*-processed matter will add additional Gd and Dy for the same total Ba (compare Fig. 2).

#### 4. SUMMARY, CONCLUSIONS, AND FUTURE WORK

We have studied neutron-capture nucleosynthesis in an AGB-intershell region under the influence of constant neutron densities ranging from *s*-process conditions with  $n = 10^7 \text{ cm}^{-3}$  up to *i*-process conditions with  $n = 10^{15} \text{ cm}^{-3}$ . At high neutron densities, the balance between neutron-capture rates and  $\beta$ -decay rates for unstable isotopes changes in a way such that the neutron-capture path can flow further away from the valley of stability. This has two main consequences: (i) the bot-

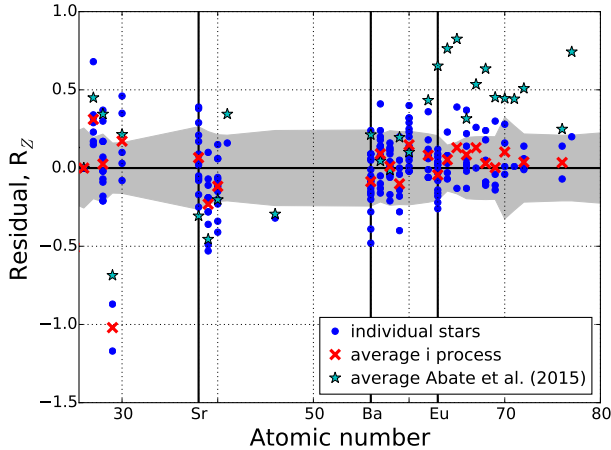


FIG. 8.— Residuals in the best-fitting models for the surface abundances of CEMP-*s/r* stars as defined in Eq. 1. The blue filled circles represent the residuals for individual stars and the average residual for each element is shown as red cross. The grey shaded area around  $R_Z = 0$  indicates the uncertainty given by the errors in the abundance measurements averaged for each element. For comparison, the cyan stars show the average residuals of the best fits from Abate et al. (2015a).

tleneck isotopes at magic neutron numbers are reached at lower atomic numbers compared to the *s* process and (ii) the majority of isotopes that are produced along the neutron-capture path are unstable. For the *i*-process abundance pattern at  $n = 10^{15} \text{ cm}^{-3}$  the former means that a large amount of unstable  $^{135}\text{I}$  with magic neutron number  $N = 50$  is produced while the latter means that all the  $^{135}\text{I}$  decays into  $^{135}\text{Ba}$  after the neutron source is switched off. While the equilibrium abundances of the ls-peak elements relative to iron are almost independent of the neutron density, the production of the hs-peak elements like Ba and *r*-process elements like Eu relative to iron increase with  $n$  and the relative abundances internally within the ls and hs peaks are also strongly modified.

Comparing the results from the models to the surface abundances of a sample of 20 CEMP-*s/r* stars shows that the observed heavy element abundance patterns of all stars but one can be convincingly reproduced. Because the *i*-process models fit the abundances of CEMP-*s/r* stars so well, we propose that this class should be re-named as CEMP-*i* stars. The majority of the best-fitting models have an abundance pattern created under the influence of a constant neutron density of  $n = 10^{14} \text{ cm}^{-3}$ .

We stress that this work uses an extremely simplistic model. The study of the influence of variations of the total neutron exposure on *i*-process abundance patterns goes beyond the scope of this work. In the future, the total neutron exposure should also be treated as a free parameter (as done for example by Roederer et al. 2016). Including constraints from the observed lead abundances of CEMP-*s/r* stars can then be used to explore the effects of the total neutron exposure on the *i* process and reveal more information about its potential physical sites. Additionally, deviations from a constant neutron-density profile need to be considered in future work, as well as additional thermal pulses with *s*-process nucleosynthesis. Moreover, a more realistic treatment (such as attempted by Abate et al. 2015b) of mass transfer and dilution in the envelopes of both the AGB star and the companion is desirable.

Uncertainties in the rates of reactions important for the *i* process were not considered in this study. Bertolli et al. (2013) studied how propagating systematic uncertainties of nuclear cross sections from different theoretical models changes the predicted abundance ratios of the hs elements and europium under *i*-process conditions. Depending on the theoretical model, changes of up to 1 dex for [Ba/La] and 0.5 dex for [La/Eu] are found (see e.g. Fig. 6 of Bertolli et al. 2013). Therefore it is important to further study the influence of nuclear physics uncertainties and their influences on the predicted abundance patterns.

Finally, in the Large and Small Magellanic Clouds, post-AGB stars of low initial mass ( $1\text{--}1.5M_{\odot}$ ) and metallicity  $[\text{Fe}/\text{H}] \approx -1$ , higher than that of CEMP-*r/s* stars, have recently been demonstrated to show abundance patterns incompatible with the *s* process (Lugaro et al. 2015). These stars should be investigated in the light of the *i* process to determine if this process is responsible for their peculiar abundances and to derive constraints on its metallicity dependence.

The authors thank Carlo Abate and Carolyn Doherty for very helpful discussion and the referee for her/his useful remarks. RJS is the recipient of a Sofja Kovalevskaja Award from the Alexander von Humboldt Foundation. ML is a Momentum (“Lendület-2014” Programme) project leader of the Hungarian Academy of Sciences.

## REFERENCES

- Abate, C., Pols, O. R., Izzard, R. G., & Karakas, A. I. 2015a, *A&A*, 581, A22
- Abate, C., Pols, O. R., Karakas, A. I., & Izzard, R. G. 2015b, *A&A*, 576, A118
- Abate, C., Stancliffe, R. J., & Liu, Z.-W. 2016, *A&A*, 587, A50
- Allen, D. M., Ryan, S. G., Rossi, S., Beers, T. C., & Tsangarides, S. A. 2012, *A&A*, 548, A34
- Aoki, W., Beers, T. C., Christlieb, N., Norris, J. E., Ryan, S. G., & Tsangarides, S. 2007, *ApJ*, 655, 492
- Aoki, W., Beers, T. C., Sivarani, T., Marsteller, B., Lee, Y. S., Honda, S., Norris, J. E., Ryan, S. G., & Carollo, D. 2008, *ApJ*, 678, 1351
- Aoki, W., Norris, J. E., Ryan, S. G., Beers, T. C., & Ando, H. 2002a, *PASJ*, 54, 933
- . 2002b, *ApJ*, 567, 1166
- Aoki, W., Ryan, S. G., Norris, J. E., Beers, T. C., Ando, H., Iwamoto, N., Kajino, T., Mathews, G. J., & Fujimoto, M. Y. 2001, *ApJ*, 561, 346
- Aoki, W., Ryan, S. G., Norris, J. E., Beers, T. C., Ando, H., & Tsangarides, S. 2002c, *ApJ*, 580, 1149
- Barbuy, B., Spite, M., Spite, F., Hill, V., Cayrel, R., Plez, B., & Petitjean, P. 2005, *A&A*, 429, 1031
- Barklem, P. S., Christlieb, N., Beers, T. C., Hill, V., Bessell, M. S., Holmberg, J., Marsteller, B., Rossi, S., Zickgraf, F.-J., & Reimers, D. 2005, *A&A*, 439, 129
- Beers, T. C. & Christlieb, N. 2005, *ARA&A*, 43, 531
- Beers, T. C., Sivarani, T., Marsteller, B., Lee, Y., Rossi, S., & Plez, B. 2007, *AJ*, 133, 1193
- Behara, N. T., Bonifacio, P., Ludwig, H.-G., Sbordone, L., González Hernández, J. I., & Caffau, E. 2010, *A&A*, 513, A72



- Bertolli, M. G., Herwig, F., Pignatari, M., & Kawano, T. 2013, ArXiv e-prints, ArXiv:1310.4578
- Bisterzo, S., Gallino, R., Straniero, O., Cristallo, S., & Käppeler, F. 2011, MNRAS, 418, 284
- , 2012, MNRAS, 422, 849
- Busso, M., Gallino, R., & Wasserburg, G. J. 1999, ARA&A, 37, 239
- Campbell, S. W. & Lattanzio, J. C. 2008, A&A, 490, 769
- Campbell, S. W., Lugaro, M., & Karakas, A. I. 2010, A&A, 522, L6
- Cohen, J. G., Christlieb, N., McWilliam, A., Shectman, S., Thompson, I., Wasserburg, G. J., Ivans, I., Dehn, M., Karlsson, T., & Melendez, J. 2004, ApJ, 612, 1107
- Cohen, J. G., Christlieb, N., Qian, Y.-Z., & Wasserburg, G. J. 2003, ApJ, 588, 1082
- Cohen, J. G., McWilliam, A., Shectman, S., Thompson, I., Christlieb, N., Melendez, J., Ramirez, S., Swensson, A., & Zickgraf, F.-J. 2006, AJ, 132, 137
- Cooke, R., Pettini, M., Steidel, C. C., Rudie, G. C., & Jorgenson, R. A. 2011, MNRAS, 412, 1047
- Cooke, R. J. & Madau, P. 2014, ApJ, 791, 116
- Cowan, J. J. & Rose, W. K. 1977, ApJ, 212, 149
- Cristallo, S., Piersanti, L., Straniero, O., Gallino, R., Domínguez, I., & Käppeler, F. 2009, PASA, 26, 139
- Cyburrt, R. H., Amthor, A. M., Ferguson, R., Meisel, Z., Smith, K., Warren, S., Heger, A., Hoffman, R. D., Rauscher, T., Sakharuk, A., Schatz, H., Thielemann, F. K., & Wiescher, M. 2010, ApJS, 189, 240
- Dardelet, L., Ritter, C., Prado, P., Heringer, E., Higgs, C., Sandalski, S., Jones, S., Denisenkov, P., Venn, K., Bertolli, M., Pignatari, M., Woodward, P., & Herwig, F. 2014, in Proceedings of XIII Nuclei in the Cosmos (NIC XIII). 7-11 July, 2014. Debrecen, Hungary., 145
- Dillmann, I., Heil, M., Käppeler, F., Plag, R., Rauscher, T., & Thielemann, F.-K. 2006, in American Institute of Physics Conference Series, Vol. 819, Capture Gamma-Ray Spectroscopy and Related Topics, ed. A. Woehr & A. Aprahamian, 123–127
- Doherty, C. L., Gil-Pons, P., Siess, L., Lattanzio, J. C., & Lau, H. H. B. 2015, MNRAS, 446, 2599
- Frebel, A., Christlieb, N., Norris, J. E., Beers, T. C., Bessell, M. S., Rhee, J., Fechner, C., Marsteller, B., Rossi, S., Thom, C., Wisotzki, L., & Reimers, D. 2006, ApJ, 652, 1585
- Frebel, A. & Norris, J. E. 2015, ARA&A, 53, 631
- Fujimoto, M. Y., Iben, Jr., I., & Hollowell, D. 1990, ApJ, 349, 580
- Fujimoto, M. Y., Ikeda, Y., & Iben, Jr., I. 2000, ApJ, 529, L25
- Gallino, R., Arlandini, C., Busso, M., Lugaro, M., Travaglio, C., Straniero, O., Chieffi, A., & Limongi, M. 1998, ApJ, 497, 388
- Goswami, A., Aoki, W., Beers, T. C., Christlieb, N., Norris, J. E., Ryan, S. G., & Tsangarides, S. 2006, MNRAS, 372, 343
- Hansen, T., Hansen, C. J., Christlieb, N., Beers, T. C., Yong, D., Bessell, M. S., Frebel, A., García Pérez, A. E., Placco, V. M., Norris, J. E., & Asplund, M. 2015, ApJ, 807, 173
- Hansen, T. T., Andersen, J., Nordström, B., Beers, T. C., Placco, V. M., Yoon, J., & Buchhave, L. A. 2016, A&A, 588, A3
- Herwig, F., Pignatari, M., Woodward, P. R., Porter, D. H., Rockefeller, G., Fryer, C. L., Bennett, M., & Hirschi, R. 2011, ApJ, 727, 89
- Herwig, F., Woodward, P. R., Lin, P.-H., Knox, M., & Fryer, C. 2014, ApJ, 792, L3
- Ivans, I. I., Sneden, C., Gallino, R., Cowan, J. J., & Preston, G. W. 2005, ApJ, 627, L145
- Johnson, J. A., Herwig, F., Beers, T. C., & Christlieb, N. 2007, ApJ, 658, 1203
- Jones, S., Ritter, C., Herwig, F., Fryer, C., Pignatari, M., Bertolli, M. G., & Paxton, B. 2016, MNRAS, 455, 3848
- Jonsell, K., Barklem, P. S., Gustafsson, B., Christlieb, N., Hill, V., Beers, T. C., & Holmberg, J. 2006, A&A, 451, 651
- Karakas, A. I. & Lattanzio, J. C. 2014, PASA, 31, 30
- Lai, D. K., Johnson, J. A., Bolte, M., & Lucatello, S. 2007, ApJ, 667, 1185
- Lau, H. H. B., Stancliffe, R. J., & Tout, C. A. 2009, MNRAS, 396, 1046
- Lee, Y. S., Beers, T. C., Masseron, T., Plez, B., Rockosi, C. M., Sobek, J., Yanny, B., Lucatello, S., Sivarani, T., Placco, V. M., & Carollo, D. 2013, aj, 146, 132
- Lucatello, S., Beers, T. C., Christlieb, N., Barklem, P. S., Rossi, S., Marsteller, B., Sivarani, T., & Lee, Y. S. 2006, ApJ, 652, L37
- Lucatello, S., Masseron, T., & Johnson, J. A. 2009, PASA, 26, 303
- Lucatello, S., Tsangarides, S., Beers, T. C., Carretta, E., Gratton, R. G., & Ryan, S. G. 2005, ApJ, 625, 825
- Lugaro, M., Campbell, S. W., & de Mink, S. E. 2009, PASA, 26, 322
- Lugaro, M., Campbell, S. W., Van Winckel, H., De Smedt, K., Karakas, A. I., & Käppeler, F. 2015, A&A, 583, A77
- Lugaro, M., Karakas, A. I., Stancliffe, R. J., & Rijs, C. 2012, ApJ, 747, 2
- Masseron, T., Johnson, J. A., Plez, B., van Eck, S., Primas, F., Goriely, S., & Jorissen, A. 2010, A&A, 509, A93
- McWilliam, A., Preston, G. W., Sneden, C., & Searle, L. 1995, AJ, 109, 2757
- Meyer, B. 2012, in Nuclei in the Cosmos (NIC XII), 96
- Mishenina, T., Pignatari, M., Carraro, G., Kovtyukh, V., Monaco, L., Korotin, S., Shereta, E., Yegorova, I., & Herwig, F. 2015, MNRAS, 446, 3651
- Norris, J. E., Ryan, S. G., & Beers, T. C. 1997, ApJ, 488, 350
- Placco, V. M., Frebel, A., Beers, T. C., Karakas, A. I., Kennedy, C. R., Rossi, S., Christlieb, N., & Stancliffe, R. J. 2013, ApJ, 770, 104
- Placco, V. M., Frebel, A., Beers, T. C., & Stancliffe, R. J. 2014, ApJ, 797, 21
- Preston, G. W. & Sneden, C. 2001, AJ, 122, 1545
- Qian, Y.-Z. & Wasserburg, G. J. 2003, ApJ, 588, 1099
- Roederer, I. U., Karakas, A. I., Pignatari, M., & Herwig, F. 2016, ApJ, 821, 37
- Sivarani, T., Bonifacio, P., Molaro, P., Cayrel, R., Spite, M., Spite, F., Plez, B., Andersen, J., Barbuy, B., Beers, T. C., Depagne, E., Hill, V., François, P., Nordström, B., & Primas, F. 2004, A&A, 413, 1073
- Sneden, C., Cowan, J. J., Lawler, J. E., Ivans, I. I., Burles, S., Beers, T. C., Primas, F., Hill, V., Truran, J. W., Fuller, G. M., Pfeiffer, B., & Kratz, K.-L. 2003a, ApJ, 591, 936
- Sneden, C., Preston, G. W., & Cowan, J. J. 2003b, ApJ, 592, 504
- Stancliffe, R. J., Dearborn, D. S. P., Lattanzio, J. C., Heap, S. A., & Campbell, S. W. 2011, ApJ, 742, 121
- Stancliffe, R. J., Glebbeek, E., Izzard, R. G., & Pols, O. R. 2007, A&A, 464, L57
- Stancliffe, R. J., Kennedy, C. R., Lau, H. H. B., & Beers, T. C. 2013, MNRAS, 435, 698
- Starkenbur, E., Shetrone, M. D., McConnachie, A. W., & Venn, K. A. 2014, MNRAS, 441, 1217
- Suda, T., Katsuta, Y., Yamada, S., Suwa, T., Ishizuka, C., Komiya, Y., Sorai, K., Aikawa, M., & Fujimoto, M. Y. 2008, PASJ, 60, 1159
- Thielemann, F.-K., Arcones, A., Käppeli, R., Liebendörfer, M., Rauscher, T., Winteler, C., Fröhlich, C., Dillmann, I., Fischer, T., Martínez-Pinedo, G., Langanke, K., Farouqi, K., Kratz, K.-L., Panov, I., & Korneev, I. K. 2011, Progress in Particle and Nuclear Physics, 66, 346
- Tuli, J. K. 2011, Nuclear Wallet Cards, 8th edition
- Van Eck, S., Goriely, S., Jorissen, A., & Plez, B. 2003, A&A, 404, 291
- Wanajo, S., Nomoto, K., Iwamoto, N., Ishimaru, Y., & Beers, T. C. 2006, ApJ, 636, 842
- Wehmeyer, B., Pignatari, M., & Thielemann, F.-K. 2015, MNRAS, 452, 1970
- Woodward, P. R., Herwig, F., & Lin, P.-H. 2015, ApJ, 798, 49
- Yong, D., Norris, J. E., Bessell, M. S., Christlieb, N., Asplund, M., Beers, T. C., Barklem, P. S., Frebel, A., & Ryan, S. G. 2013, ApJ, 762, 27
- Zijlstra, A. A. 2004, MNRAS, 348, L23

APPENDIX  
 $\alpha$  DECAY RATES

TABLE 3  
 IN THE NETWORK INCLUDED NUCLEAR DECAY DATA FROM TULI (2011).

Decay	$t_{1/2}$ (s)	Decay Ratio (%)	Decay Rate ( $s^{-1}$ )
${}^5\text{He} \rightarrow n + {}^4\text{He}$	$6.00 \times 10^{-25}$	100	$1.16 \times 10^{24}$
${}^{144}\text{Nd} \rightarrow {}^{140}\text{Ce} + {}^4\text{He}$	$7.22 \times 10^{22}$	100	$9.60 \times 10^{-24}$
${}^{145}\text{Pm} \rightarrow {}^{141}\text{Pr} + {}^4\text{He}$	$5.58 \times 10^8$	$2.80 \times 10^{-7}$	$3.48 \times 10^{-18}$
${}^{146}\text{Sm} \rightarrow {}^{142}\text{Nd} + {}^4\text{He}$	$3.25 \times 10^{15}$	100	$2.13 \times 10^{-16}$
${}^{147}\text{Sm} \rightarrow {}^{143}\text{Nd} + {}^4\text{He}$	$3.34 \times 10^{18}$	100	$2.07 \times 10^{-19}$
${}^{148}\text{Sm} \rightarrow {}^{144}\text{Nd} + {}^4\text{He}$	$2.21 \times 10^{23}$	100	$3.14 \times 10^{-24}$
${}^{150}\text{Gd} \rightarrow {}^{146}\text{Sm} + {}^4\text{He}$	$5.64 \times 10^{13}$	100	$1.23 \times 10^{-14}$
${}^{151}\text{Gd} \rightarrow {}^{147}\text{Sm} + {}^4\text{He}$	$1.07 \times 10^7$	$8.00 \times 10^{-7}$	$5.18 \times 10^{-16}$
${}^{152}\text{Gd} \rightarrow {}^{148}\text{Sm} + {}^4\text{He}$	$3.41 \times 10^{21}$	100	$2.04 \times 10^{-22}$
${}^{152}\text{Dy} \rightarrow {}^{148}\text{Gd} + {}^4\text{He}$	$8.57 \times 10^3$	0.1	$8.09 \times 10^{-8}$
${}^{153}\text{Dy} \rightarrow {}^{149}\text{Gd} + {}^4\text{He}$	$2.30 \times 10^4$	$9.40 \times 10^{-3}$	$2.83 \times 10^{-9}$
${}^{154}\text{Dy} \rightarrow {}^{150}\text{Gd} + {}^4\text{He}$	$9.46 \times 10^{13}$	100	$7.33 \times 10^{-15}$
${}^{187}\text{Re} \rightarrow {}^{183}\text{Ta} + {}^4\text{He}$	$1.37 \times 10^{18}$	$1.00 \times 10^{-4}$	$5.08 \times 10^{-25}$
${}^{210}\text{Pb} \rightarrow {}^{206}\text{Hg} + {}^4\text{He}$	$7.00 \times 10^8$	$1.90 \times 10^{-6}$	$1.88 \times 10^{-17}$
${}^{210}\text{Bi} \rightarrow {}^{206}\text{Tl} + {}^4\text{He}$	$4.33 \times 10^5$	$1.30 \times 10^{-4}$	$2.08 \times 10^{-12}$
${}^{211}\text{Bi} \rightarrow {}^{207}\text{Tl} + {}^4\text{He}$	$1.28 \times 10^2$	99.72	$5.38 \times 10^{-3}$
${}^{212}\text{Bi} \rightarrow {}^{208}\text{Tl} + {}^4\text{He}$	$3.63 \times 10^3$	35.94	$6.86 \times 10^{-5}$
${}^{213}\text{Bi} \rightarrow {}^{209}\text{Tl} + {}^4\text{He}$	$2.74 \times 10^3$	2.2	$5.57 \times 10^{-6}$
${}^{214}\text{Bi} \rightarrow {}^{210}\text{Tl} + {}^4\text{He}$	$1.19 \times 10^3$	0.02	$1.16 \times 10^{-7}$
${}^{210}\text{Po} \rightarrow {}^{206}\text{Pb} + {}^4\text{He}$	$1.20 \times 10^7$	100	$5.80 \times 10^{-8}$
${}^{211}\text{Po} \rightarrow {}^{207}\text{Pb} + {}^4\text{He}$	$5.16 \times 10^{-1}$	100	1.34
${}^{212}\text{Po} \rightarrow {}^{208}\text{Pb} + {}^4\text{He}$	$2.99 \times 10^{-7}$	100	$2.32 \times 10^6$
${}^{213}\text{Po} \rightarrow {}^{209}\text{Pb} + {}^4\text{He}$	$3.72 \times 10^{-6}$	100	$1.86 \times 10^5$
${}^{214}\text{Po} \rightarrow {}^{210}\text{Pb} + {}^4\text{He}$	$1.64 \times 10^{-4}$	100	$4.22 \times 10^3$
${}^{215}\text{Po} \rightarrow {}^{211}\text{Pb} + {}^4\text{He}$	$1.78 \times 10^{-3}$	100	$3.89 \times 10^2$
${}^{216}\text{Po} \rightarrow {}^{212}\text{Pb} + {}^4\text{He}$	$1.45 \times 10^{-1}$	100	4.78
${}^{217}\text{Po} \rightarrow {}^{213}\text{Pb} + {}^4\text{He}$	1.53	100	$4.53 \times 10^{-1}$
${}^{218}\text{Po} \rightarrow {}^{214}\text{Pb} + {}^4\text{He}$	$1.86 \times 10^2$	99.98	$3.73 \times 10^{-3}$

## TABLES

TABLE 4  
FINAL  $[X/Fe]$  FOR THE SIMULATIONS WITH DIFFERENT NEUTRON DENSITIES  $n$ .

Z	element	Neutron density in $\text{cm}^{-3}$			
		$10^{12}$	$10^{13}$	$10^{14}$	$10^{15}$
26	Fe	0.00	0.00	0.00	0.00
27	Co	1.76	1.92	2.02	1.90
28	Ni	1.43	1.60	1.71	1.60
29	Cu	2.55	2.75	2.89	2.80
30	Zn	2.36	2.86	3.22	3.13
31	Ga	3.08	3.36	3.58	3.71
32	Ge	3.16	3.38	3.61	3.73
33	As	3.21	3.73	4.06	4.33
34	Se	3.40	3.77	4.28	4.29
35	Br	3.33	3.64	4.01	4.09
36	Kr	4.79	4.94	5.04	4.90
37	Rb	4.66	4.79	4.84	4.81
38	Sr	4.31	4.32	4.35	4.37
39	Y	4.52	4.65	4.58	4.64
40	Zr	4.74	4.90	5.02	4.88
41	Nb	4.54	4.64	5.05	5.25
42	Mo	4.80	5.16	5.33	5.25
44	Ru	4.51	4.72	4.96	5.04
45	Rh	4.32	4.47	4.67	4.82
46	Pd	4.80	5.03	5.16	5.02
47	Ag	4.22	4.48	4.70	4.85
48	Cd	4.78	5.05	5.19	5.06
49	In	4.86	5.03	5.13	5.10
50	Sn	5.11	5.30	5.40	5.25
51	Sb	5.08	5.26	5.36	5.24
52	Te	4.96	5.24	5.40	5.40
53	I	4.65	5.18	5.47	5.44
54	Xe	5.36	5.87	6.06	6.14
55	Cs	4.98	5.37	6.04	6.53
56	Ba	5.42	5.55	6.06	6.57
57	La	5.38	5.53	5.66	5.59
58	Ce	5.12	5.36	5.76	5.72
59	Pr	5.30	5.40	5.81	5.87
60	Nd	5.39	5.54	5.63	5.57
62	Sm	5.10	5.30	5.65	5.75
63	Eu	4.79	5.16	5.48	5.56
64	Gd	5.05	5.36	5.63	5.63
65	Tb	4.85	5.00	5.13	5.35
66	Dy	4.88	5.01	5.31	5.41
67	Ho	4.76	5.02	5.18	5.22
68	Er	5.29	5.54	5.72	5.78
69	Tm	5.14	5.32	5.60	5.80
70	Yb	5.61	5.80	5.85	5.80
71	Lu	5.24	5.57	5.99	5.90
72	Hf	5.54	5.80	6.04	6.00
73	Ta	5.88	6.03	6.06	6.12
74	W	5.59	5.90	6.10	6.16
75	Re	5.46	5.69	5.88	5.90
76	Os	5.14	5.31	5.37	5.35
77	Ir	4.35	4.56	4.83	4.91
78	Pt	4.95	5.17	5.37	5.33
79	Au	4.78	4.97	5.20	5.19
80	Hg	5.73	6.02	6.32	6.28

TABLE 5  
 DETAILS ABOUT THE 20 CEMP-*s/r* STARS IN THE SAMPLE OF ABATE ET AL. (2015A): SURFACE GRAVITIES, TEMPERATURES AND SELECTED CHEMICAL PROPERTIES.

ID	$\log(g/\text{cm s}^{-2})$	$T_{\text{eff}}$ (K)	Number of observed elements	[Fe/H]	[C/Fe]	[Ba/Fe]	[Eu/Fe]	Reference
BS16080-175	3.7(2)	6240	6	-1.9	1.8	1.6	1.1	1
BS17436-058	2.7(2)	5690	7	-1.8	1.6	1.7	1.2	1
CS22881-036	4.0(1)	6200	14	-2.1	2.1	1.9	1.0	23
CS22898-027	3.7(3)	6110	22	-2.3	2.0	2.3	2.0	3, 4, 18, 20
CS22948-027	1.8(4)	4800	21	-2.5	2.4	2.4	1.9	5, 7
CS29497-030	4.0(5)	6966	33	-2.5	2.4	2.3	1.7	15, 16, 24
CS29526-110	3.2(1)	6500	18	-2.4	2.3	2.1	1.8	3, 4
CS31062-012	4.2(4)	6099	24	-2.8	2.3	2.1	1.6	2, 3, 4, 6, 21
CS31062-050	2.9(3)	5489	37	-2.5	1.9	2.4	2.0	2, 3, 4, 6
HD187861	2.0(4)	4960	14	-2.4	2.0	1.9	1.3	19, 26
HD224959	1.9(3)	5050	14	-2.1	1.8	2.2	1.7	19
HE0131-3953	3.8(1)	5928	16	-2.7	2.5	2.2	1.7	8
HE0143-0441	4.0(4)	6305	22	-2.4	2.0	2.4	1.7	12, 13
HE0338-3945	4.1(4)	6161	32	-2.5	2.1	2.4	2.0	8, 17
HE1105+0027	3.5(1)	6132	16	-2.5	2.0	2.4	1.9	8
HE1305+0007	1.5(5)	4655	21	-2.2	2.1	2.6	2.2	9, 14
HE2148-1247	3.9(1)	6380	25	-2.4	2.0	2.4	2.0	11
HE2258-6358	1.6(1)	4900	31	-2.7	2.4	2.3	1.7	22
LP625-44	2.6(3)	5500	31	-2.8	2.3	2.8	1.9	2, 4, 21
SDSSJ0912+0216	4.5(1)	6500	28	-2.6	2.3	1.6	1.3	10

REFERENCES. — (1) Allen et al. 2012; (2) Aoki et al. 2001; (3) Aoki et al. 2002c; (4) Aoki et al. 2002a; (5) Aoki et al. 2007; (6) Aoki et al. 2008; (7) Barbay et al. 2005; (8) Barklem et al. 2005; (9) Beers et al. 2007; (10) Behara et al. 2010; (11) Cohen et al. 2003; (12) Cohen et al. 2004; (13) Cohen et al. 2006; (14) Goswami et al. 2006; (15) Ivans et al. 2005; (16) Johnson et al. 2007; (17) Jonsell et al. 2006; (18) Lai et al. 2007; (19) Masseron et al. 2010; (20) McWilliam et al. 1995; (21) Norris et al. 1997; (22) Placco et al. 2013; (23) Preston & Sneden 2001; (24) Sivarani et al. 2004; (25) Sneden et al. 2003b; (26) Van Eck et al. 2003

## ALL FITS

This section shows the best fitting models for each of the 20 CEMP-*s/r* stars. Details of each best fit (neutron density  $n$ ,  $\chi^2$  and dilution factor  $d$ ) are shown in the right corner of the plots. The lower panel shows the distribution of the residuals. The uncertainty of the observations  $\sigma_{Z,\text{obs}}$  is indicated by errorbars in the upper panel and by the shaded region in the lower panel. The vertical lines show the location of Sr, Ba and Eu which are representatives of the ls and hs peak as well as the *r* process, respectively. We note that the abundance patterns reported by Behara et al. (2010) for SDSSJ0912+0216 (as well as SDSSJ1349-0229, which is not included in the sample of Abate et al. (2015a) because of the low  $[\text{Fe}/\text{H}]$ ) are at odds with any *s* or *i*-process models and need an independent verification.

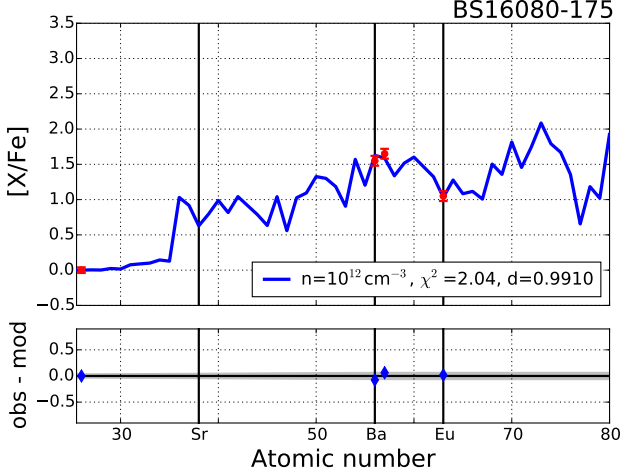


FIG. 9.— Best fitting model for CEMP-*s/r* star BS16080-175. The best fitting *s*-process models with initial *r*-process enhancement can be found in Fig. 5 from Bisterzo et al. (2012).

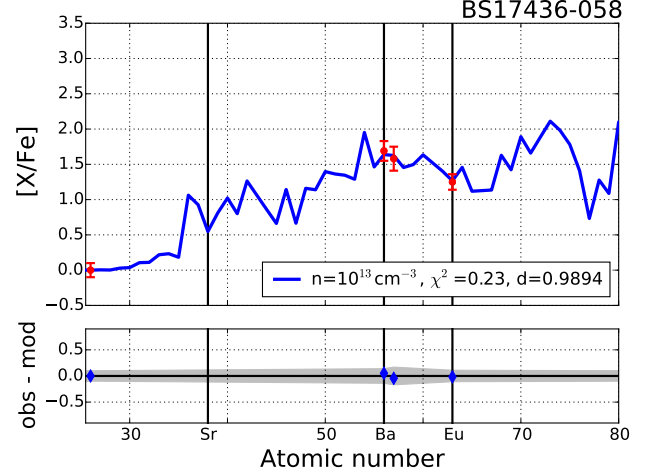


FIG. 10.— Best fitting model for CEMP-*s/r* star BS17436-058. The best fitting *s*-process models with initial *r*-process enhancement can be found in Fig. 16 from Bisterzo et al. (2012).

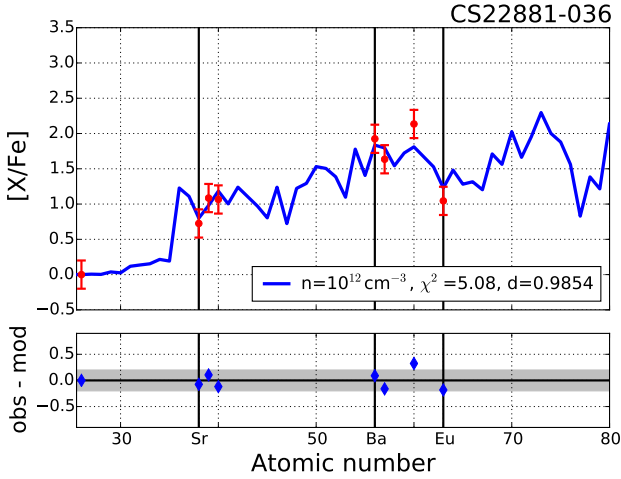


FIG. 11.— Best fitting model for CEMP-*s/r* star CS22881-036. The best fitting *s*-process models with initial *r*-process enhancement can be found in Fig. 1 from Bisterzo et al. (2012).

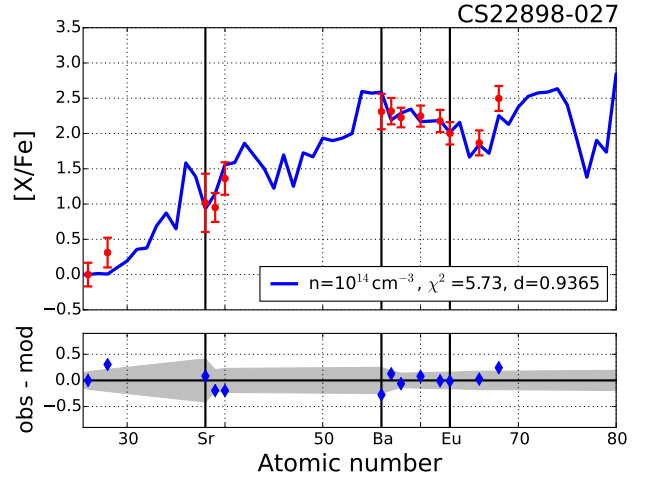


FIG. 12.— Best fitting model for CEMP-*s/r* star CS22898-027. The best fitting *s*-process models with initial *r*-process enhancement can be found in Fig. 17 from Bisterzo et al. (2012) and with binary evolution in Fig. 5 from Abate et al. (2015a).



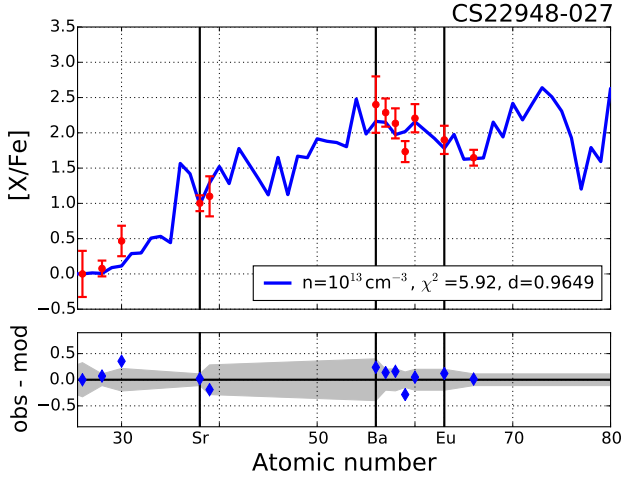


FIG. 13.— Best fitting model for CEMP-*s/r* star CS22948-027. The best fitting *s*-process models with initial *r*-process enhancement can be found in Fig. 27 from Bisterzo et al. (2012) and with binary evolution in Fig. A2 from Abate et al. (2015b).

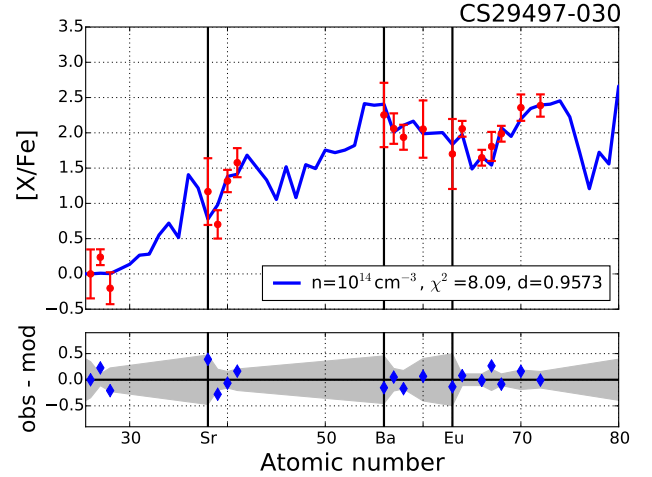


FIG. 14.— Best fitting model for CEMP-*s/r* star CS29497-030. The best fitting *s*-process models with initial *r*-process enhancement can be found in Fig. 18 from Bisterzo et al. (2012) and with binary evolution in Fig. 6 from Abate et al. (2015b).

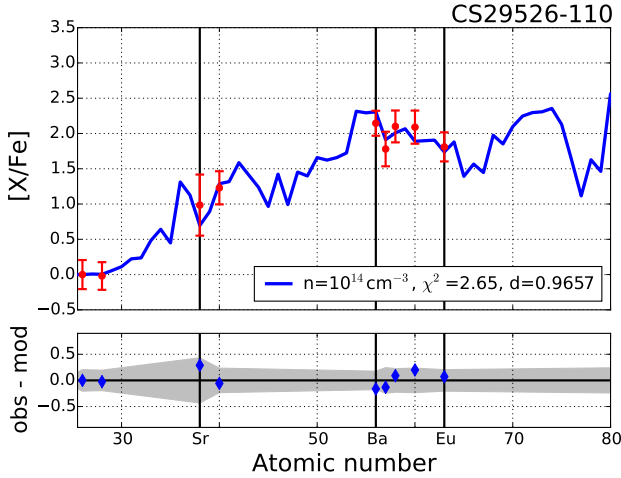


FIG. 15.— Best fitting model for CEMP-*s/r* star CS29526-110. The best fitting *s*-process models with initial *r*-process enhancement can be found in Fig. 23 from Bisterzo et al. (2012).

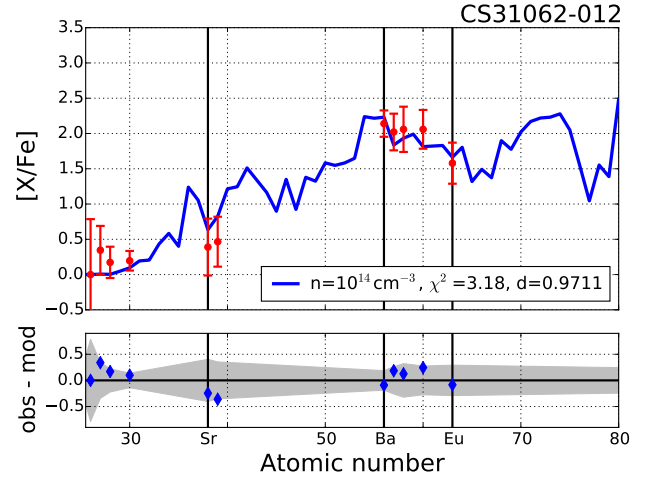


FIG. 16.— Best fitting model for CEMP-*s/r* star CS31062-012. The best fitting *s*-process models with initial *r*-process enhancement can be found in Fig. 24 from Bisterzo et al. (2012).

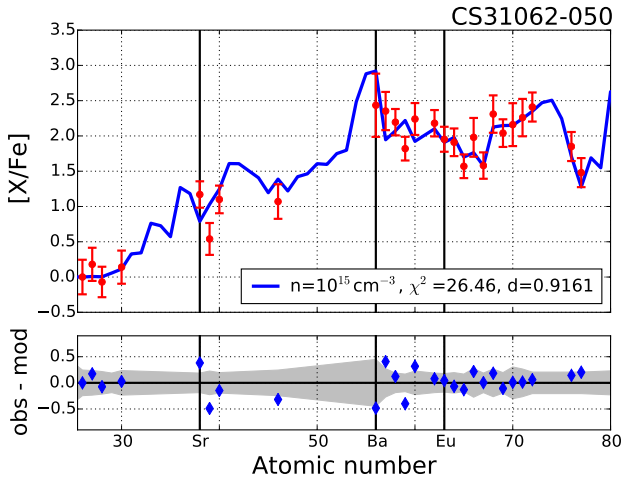


FIG. 17.— Best fitting model for CEMP-*s/r* star CS31062-050. The best fitting *s*-process models with initial *r*-process enhancement can be found in Fig. 26 from Bisterzo et al. (2012).

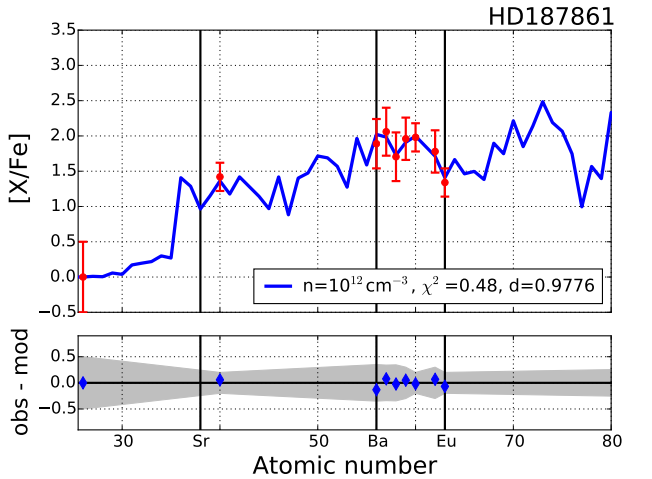


FIG. 18.— Best fitting model for CEMP-*s/r* star HD187861. The best fitting *s*-process models with initial *r*-process enhancement can be found in Fig. 29 from Bisterzo et al. (2012).

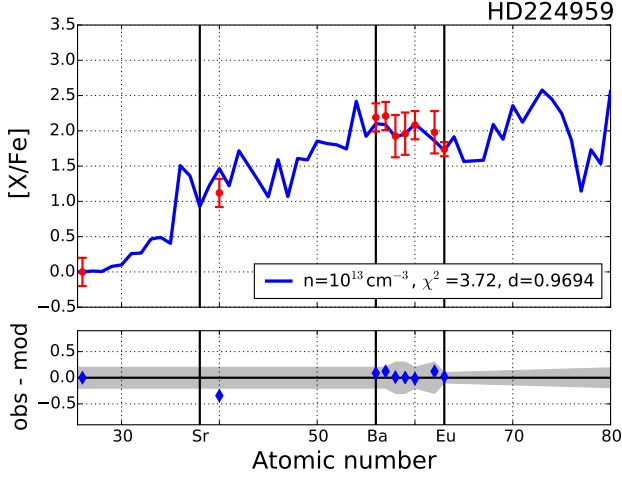


FIG. 19.— Best fitting model for CEMP-*s/r* star HD224959. The best fitting *s*-process models with initial *r*-process enhancement can be found in Fig. 30 from Bisterzo et al. (2012) and with binary evolution in Fig. A8 from Abate et al. (2015b).

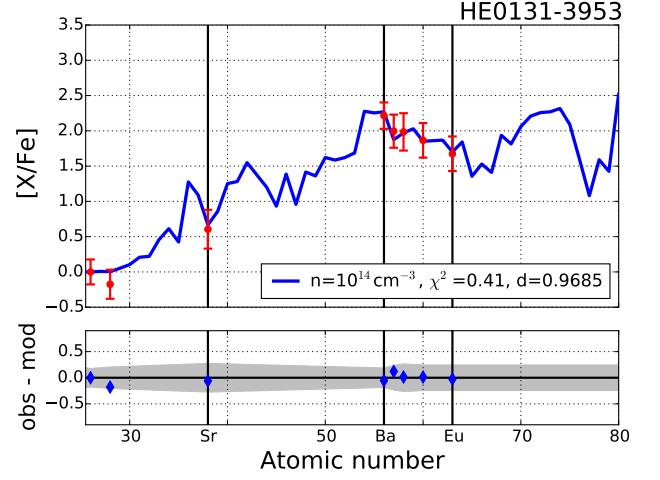


FIG. 20.— Best fitting model for CEMP-*s/r* star HE0131-3953. The best fitting *s*-process models with initial *r*-process enhancement can be found in Fig. A8 from Bisterzo et al. (2012).

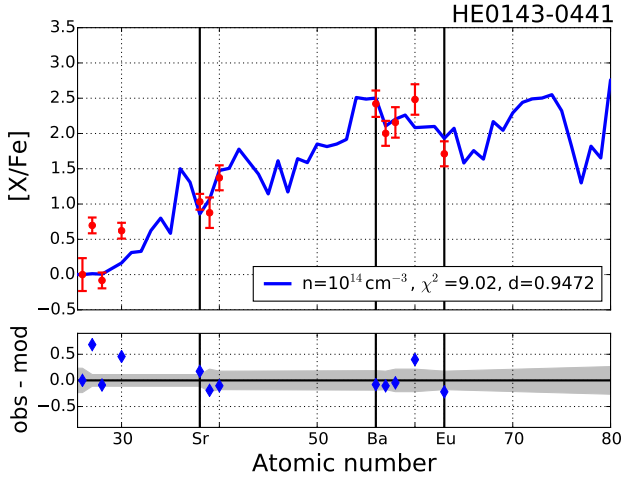


FIG. 21.— Best fitting model for CEMP-*s/r* star HE0143-0441. The best fitting *s*-process models with initial *r*-process enhancement can be found in Fig. 33 from Bisterzo et al. (2012).

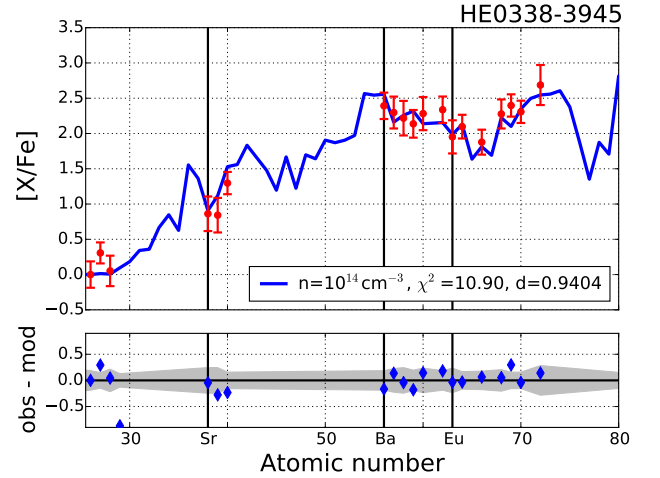


FIG. 22.— Best fitting model for CEMP-*s/r* star HE0338-3945. The best fitting *s*-process models with initial *r*-process enhancement can be found in Fig. 19 from Bisterzo et al. (2012).

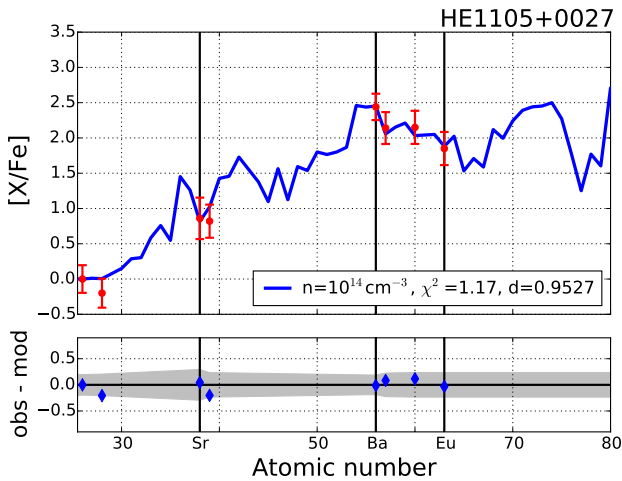


FIG. 23.— Best fitting model for CEMP-*s/r* star HE1105+0027. The best fitting *s*-process models with initial *r*-process enhancement can be found in Fig. 20 from Bisterzo et al. (2012).

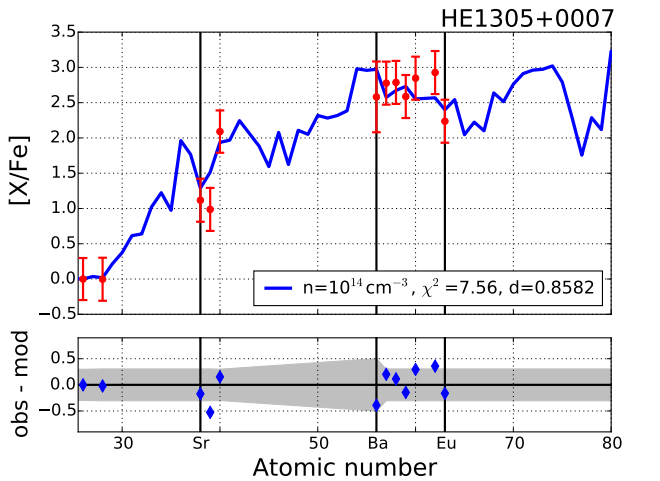


FIG. 24.— Best fitting model for CEMP-*s/r* star HE1305+0007. The best fitting *s*-process models with initial *r*-process enhancement can be found in Fig. 22 from Bisterzo et al. (2012).

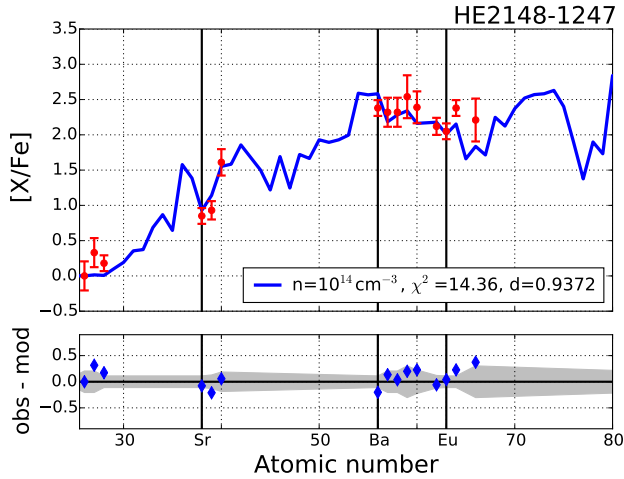


FIG. 25.— Best fitting model for CEMP-*s/r* star HE2148-1247. The best fitting *s*-process models with initial *r*-process enhancement can be found in Fig. 21 from Bisterzo et al. (2012).

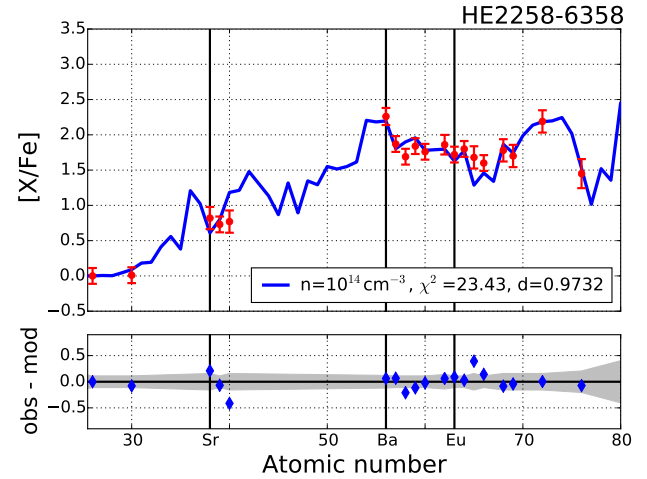


FIG. 26.— Best fitting model for CEMP-*s/r* star HE2258-6358.

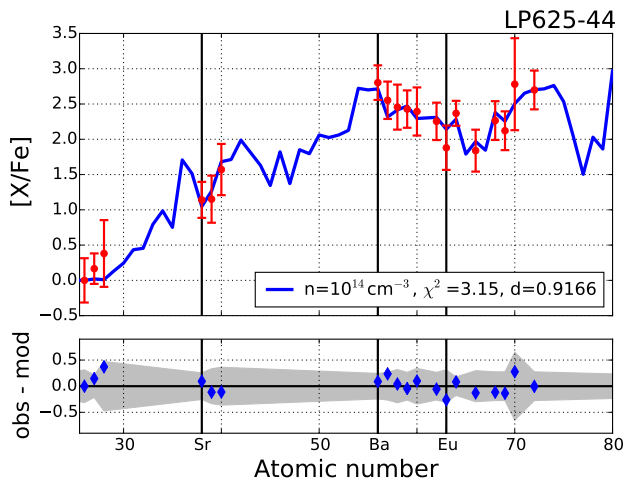


FIG. 27.— Best fitting model for CEMP-*s/r* star LP625-44. The best fitting *s*-process models with initial *r*-process enhancement can be found in Fig. 31 from Bisterzo et al. (2012) and with binary evolution in Fig. A11 from Abate et al. (2015b).

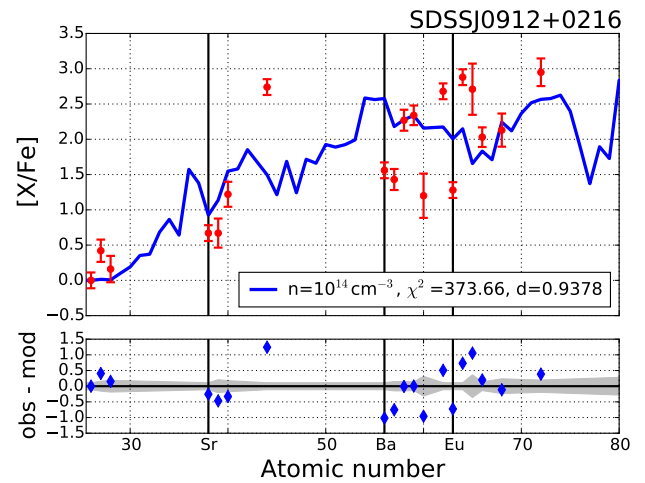


FIG. 28.— Best fitting model for CEMP-*s/r* star SDSSJ0912+0216. The best fitting *s*-process models with initial *r*-process enhancement can be found in Fig. 34 from Bisterzo et al. (2012).